THE ASTROPHYSICAL JOURNAL, 561:396–405, 2001 November 1

RECONCILING EXTREME-ULTRAVIOLET AND RADIO OBSERVATIONS OF THE SUN'S CORONA

J. ZHANG,[1] M. R. KUNDU,[2] S. M. WHITE,[2] K. P. DERE,[3] AND J. S. NEWMARK[3]

Received 2000 December 4; accepted 2001 July 2

ABSTRACT

The Sun's corona, which is composed of plasma at a temperature of a few millions of degrees, can be best viewed in two electromagnetic domains, one from wavelengths of a few angstroms to hundreds of angstroms (in the soft X-ray and EUV domain), the other from wavelengths of a few centimeters to several tens of centimeters (in the radio domain). In this paper, we present a quantitative comparison of coronal observations made in these two domains with high spatial resolution over the full disk of the Sun. The EUV observations were taken with the EIT (Extreme-Ultraviolet Imaging Telescope) on board *SOHO* (*Solar and Heliospheric Observatory*), and the radio observations were taken with the VLA (Very Large Array). The two sets of images show very similar morphologies, indicating that the different wavelengths originate from common solar features. We predict radio fluxes using the temperature and emission measure of the corona calculated from EIT observations, adopting Meyer's table of coronal abundances for the calculations. In each of the seven observations investigated, there always exists a good linear correlation in the pixel-by-pixel correlation plot between the predicted and the observed radio flux for coronal features over a wide range of flux variation. Nevertheless, the predicted radio flux is systematically larger than that observed by a factor of 2.0 ± 0.2, on average. We attribute the difference to the underestimation of the abundance of Fe relative to H in the abundances adopted by Meyer. On this basis, we place the absolute Fe abundance in the corona at 7.8×10^{-5}, which has an enrichment factor of 2.4 relative to the accepted photospheric Fe abundance.

Subject headings: Sun: abundances — Sun: atmosphere — Sun: corona — Sun: radio radiation — Sun: UV radiation

1. INTRODUCTION

The purpose of this paper is to reconcile EUV and radio observations of the Sun's corona. Such reconciliation is an important step for diagnosing coronal magnetic fields and other important physical parameters of the corona using current observations. Direct observations of coronal magnetic fields may hold the key to many solar mysteries, such as coronal heating and solar flares. The most powerful technique for their study is to exploit combined radio and EUV/soft X-ray observations. The radio (wavelengths from a few centimeters to several tens of centimeters) and EUV/soft X-ray (wavelengths from a few angstroms to hundreds of angstroms) are the two best spectral windows to observe the million-degree coronal plasma, and they complement each other in diagnostic capability (White 1999). The radio emission of the corona, through thermal bremsstrahlung and/or gyroresonance emission of free electrons, is sensitive to temperature and emission measure, as well as to magnetic field in the corona. On the other hand, the EUV/soft X-ray emission, mainly through line emission of highly ionized ions of trace elements, provides information on temperature and emission measure, as well as on abundances in the corona.

A great deal of effort has been put into this approach. However, the results have not always been satisfactory: difficulties were often found in reconciling these two sets of observations. In a series of papers based on the coronal magnetic structure observing campaign in 1987 (Nitta et al. 1991; Brosius et al. 1992; Schmelz et al. 1992, 1994), it has been shown that the predicted radio flux, calculated from the temperature and emission measure observed with the X-ray Polychromator aboard *Solar Maximum Mission* (*SMM*), was always higher than that directly observed by the VLA (Very Large Array) by a factor of 2–4. To account for the discrepancy, the authors suggested that there exists a significant amount of cool material ($< 5.0 \times 10^5$ K) above the hot, soft X-ray–emitting plasma. A similar scenario was proposed earlier by Webb et al. (1987). Klimchuk & Gary (1995) found that the temperature and emission measures derived from observations with the Soft X-ray Telescope (SXT) on board *Yohkoh* were ~ 2.5 times greater than the corresponding values derived from spectrally resolved microwave data from the Owens Valley Radio Observatory.

One plausible explanation of the discrepancy is that the coronal elemental abundance used in the calculation is not correct. The studies mentioned above used Meyer's coronal abundance (Meyer 1985) to derive the coronal emission measure and predict the radio flux. However, different versions of coronal abundances have been proposed. There is a well-known FIP (first ionization potential) effect, such that elements in the corona with low FIP (< 10.5 eV) are more abundant than elements with high FIP by a factor of about 4, compared with their distributions in the photosphere. Different versions of coronal abundance agree with the FIP effect but vary in how much the low-FIP elements are enriched or high-FIP elements are depleted. They can be simply classified into three models based on the enrichment factor of low-FIP elements: low-enrichment model (factor about 1; Meyer 1985), high-enrichment model (factor about 4; Feldman 1992; Meyer 1993), and intermediate-enrichment model (factor about 2; Fludra & Schmelz 1999). Regarding the element Fe, a good representative of the low-FIP elements and a major contributor to the coronal EUV/soft X-ray emission, its abundance in the corona has been proposed to be higher than the accepted photospheric

[1] Center for Earth Observing and Space Research, School of Computational Science, George Mason University, Fairfax, VA 22030.
[2] Astronomy Department, University of Maryland, College Park, MD 20742.
[3] E. O. Hulburt Center for Space Research, Naval Research Laboratory, Washington, DC 20375.

value (3.23×10^{-5}; Anders & Grevesse 1989) by factors of 1.2 (Meyer 1985), 3.9 (Feldman 1992), 9.8 (Waljeski et al. 1994), 1.4 (Fludra & Schmelz 1999), and 4.8 (White et al. 2000). By adjusting the coronal elemental abundance, the discrepancy between the predicted and observed radio flux can be reconciled; as the assumed abundance increases, the hydrogen emission measure required to produce the observed EUV/X-ray line emission decreases, and thus the predicted radio flux decreases. White et al. (2000) used the discrepancy between the predicted and observed radio flux to determine the coronal Fe abundance. Brosius et al. (1997) showed that the variations in the coronal elemental abundances could affect the determination of the microwave emission mechanism and thus change the coronal magnetic field strengths derived from radio data.

In this paper, we compare EUV and radio observations of the corona based on an improved data set. The EUV observations were made by the EIT (Extreme-Ultraviolet Imaging Telescope; Delaboudinière et al. 1995; Moses et al. 1997) on board *SOHO* (*Solar and Heliospheric Observatory*), while the radio observations were made at two wavelengths, 20 cm (1.46 GHz) and 6 cm (4.6 GHz), by the VLA. Both EUV and radio observations provide spatially resolved coronal images over a large field of view. Compared with previous studies, our data sets have three advantages. (1) We have larger samples of radio observations, making a statistical study possible. (2) The high spatial resolution and sensitivity of EIT images enable us to make the comparison on a pixel-by-pixel basis, which not only further increases the statistical significance but also enables us to differentiate radio thermal bremsstrahlung emission from gyroresonance emission. (3) EUV observations are sensitive to the coronal plasma in the temperature range 1–3 MK, which dominates the emission measure of the quiescent corona, unlike soft X-ray data, which are usually more sensitive to plasma hotter than this, where the emission measure is less. In § 2, we describe the instruments and the selection of the data. In § 3, we make a quantitative comparison between the EUV and radio observations. In § 4, we discuss issues raised by the reconciliation of the EUV and radio observations, especially the coronal Fe abundance. Section 5 summarizes our conclusions.

2. INSTRUMENTS AND DATA SELECTION

The EIT observes the Sun's atmosphere in four EUV passbands centered at 171, 195, 284, and 304 Å, whose peak response temperatures are 0.8, 1.2, 1.9, and 0.08 MK, respectively (based on recent EIT preflight calibration by Dere et al. 2000). The emission in the first three passbands, which are sensitive to coronal temperatures, is mainly bound-bound emission of Fe ions in different ionization stages: Fe IX/Fe X, Fe XII, and Fe XV, respectively. The emission in the fourth passband, which is sensitive to transition region temperatures, is mainly from He II. In this paper, we will only use the observations of the three coronal passbands. In each passband, the Sun's images are taken on an EUV–sensitive 1024×1024 format charge-coupled device (CCD) camera with a pixel size of 2.″6 and a field of view of $45' \times 45'$. Since the launch of *SOHO* in 1995 December, the EIT has been taking excellent coronal images on a regular basis. The synoptic observations consist of full-disk, full-resolution images in four passbands quasi-simultaneously (within 20 minutes) every 6 hr. The CME (coronal mass ejection) watch plan takes images in the 195 Å passband about every 15 minutes. Thus, the EIT observations provide coverage of almost any long-lived feature in the corona. This data set is very valuable for many general purpose studies, including the comparison with radio images presented in this paper.

The radio images were made with the VLA at 6 and 20 cm. The solar group at the University of Maryland has accumulated several sets of VLA solar observations. In 1996 and 1997, there were nine days of observations: 1996 June 29, July 4, and July 6 and 1997 June 27, June 29, June 30, July 27, August 3, and November 11. In this paper, we make use of the observations on three days: 1996 June 29 and July 6 and 1997 November 11. The other six days' observations are not suitable for the quantitative studies pursued here, for the following reasons. For 1996 July 4, the EIT observations lack images in the 284 Å passband, resulting in an insufficient determination of emission measure in the corona. For observations on 1997 June 27, 29, and 30, the Sun is so quiet that there are no bright features or active regions on the disk. For 1997 July 27, EIT observations are not available because of a routine bake-out operation carried out in order to restore the CCD's sensitivity. On 1997 August 3, the VLA was in its C configuration, which has a maximum antenna separation of 3.6 km and may result in missing radio flux; this issue will be explored in § 3.

For the observations investigated in this paper, the VLA was in its D configuration, which has a maximum antenna separation of only 1 km. In this configuration, the observations at 20 cm (L band) result in an effective field of view of about 30′ and a spatial resolution of about 50″, while the 6 cm (C band) observations have an effective field of view of 9′ and a spatial resolution about 14″. The VLA 20 cm images are deconvolved using a disk with brightness temperature 10^5 K as a default image. At 6 cm, the data contain no information on spatial scales of the size of the solar disk, so this disk component is absent from the 6 cm radio images. A VLA solar observation usually lasts about 10 hr, from about 13 to 23 UT.

3. OBSERVATIONAL RESULTS

We use the observations on 1997 November 11 as an example to illustrate data reduction and analysis. The results for the other two days' observations are also presented in this section.

3.1. *1997 November 11 Observations*

3.1.1. *Making Model Radio Images from EIT Observations*

A set of EIT synoptic coronal images (at 171, 195, and 284 Å) is shown in Figure 1. The images were taken at 19:24, 19:36, and 19:30 UT on 1997 November 11, with exposure times of 5.7, 9.0, and 62.0 s, respectively. Because these images were taken within 12 minutes, the spatial alignment between them has been well preserved. The appearance of these images is similar at all wavelengths. These images can be used to derive the temperature and emission measure distribution of the corona. Using the latest EIT in-flight calibration (Newmark et al. 2001, private communication), we fit the three images to a two–temperature-component coronal model using the method described by Zhang, White, & Kundu (1999). The tradi-

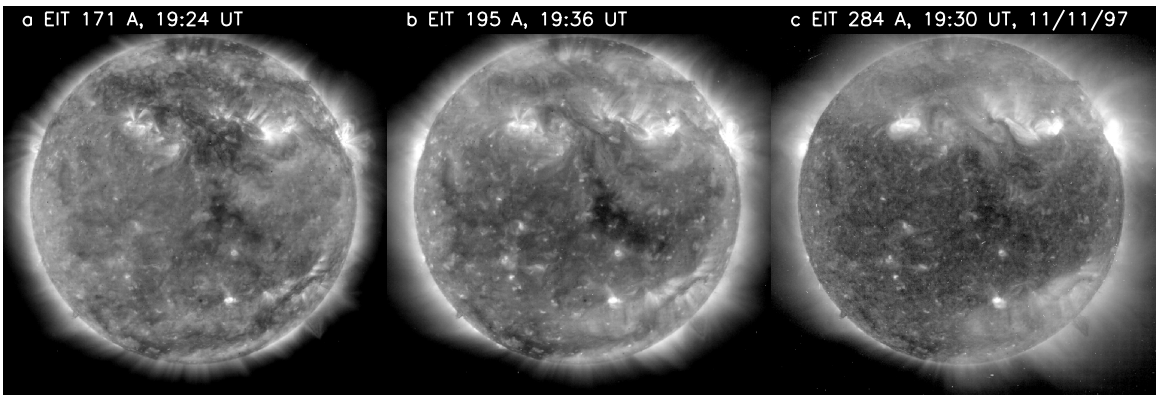

FIG. 1.—Three EIT coronal images observed at (*a*) 171 Å, (*b*) 195 Å, and (*c*) 284 Å on 1997 November 11. The Sun's north is to the top, and east is to the left.

tional image ratio method, which uses a pair of images to derive a single temperature for the corona, is not adequate to restore the information presented by a set of three coronal images. Specifically, the emission measure derived may be underestimated by a factor of 2; e.g., from a pair of EIT 171 and 195 Å images only, the solution of the one-temperature model only retrieves the emission measure of the plasma in the temperature range from 0.6 to 1.6 MK, to which the EIT 171 and 195 Å images are sensitive. On the other hand, using a two-temperature model that includes 284 Å images, one can determine the emission measure of the plasma in the temperature range from 0.6 to 2.8 MK, which covers the bulk of the quiescent corona. The method used effectively minimizes the total emission measure needed to reproduce the images in the three wavelengths (Zhang et al. 1999).

In converting the observed EUV photon counts to coronal hydrogen emission measures, we use the coronal abundance adopted by Meyer (1985), in which $N_{\rm Fe}/N_{\rm H} = 3.89 \times 10^{-5}$ (or $\log A_{\rm Fe} = 7.59$); this abundance has been often used as the default in the analysis software for *Yohkoh*/SXT and *SOHO*/EIT. The atomic data are from the CHIANTI database (Dere et al. 1997) and the ionization equilibrium calculations are from Arnaud & Raymond (1992). In each pixel in the EIT image, we determine the temperature and emission measure of both a hot and a cool thermal plasma component, so that the EIT 171, 195, and 284 Å fluxes are reproduced. We find that the range of T_C (temperature of cool component) solutions for all disk pixels is from 0.8 to 1.4 MK, while T_H (temperature of hot component) ranges from 1.6 to 2.8 MK. The range of $\rm EM_C$ (emission measure of cool component) for all disk pixels is from 1.0×10^{26} to 1.0×10^{28} cm^{-5}, while $\rm EM_H$ (emission measure of hot component) ranges from 1.5×10^{26} to 1.6×10^{29} cm^{-5}. (For a general discussion of the properties of the resulting temperature and emission measure maps, please refer to Zhang et al. 1999). Because the emission measure varies by 3 orders of magnitude among coronal features and the temperature lies within a limited range of a factor of 2, it is expected that the derived radio flux would be primarily determined by the emission measure rather than by the temperature.

With known temperature and emission measure, we can now predict the radio flux at a given frequency (or wavelength). The optical depth τ of thermal bremsstrahlung (or free-free) emission can be expressed as

$$\tau_{\rm ff} = 9.8 \times 10^{-3}(\nu \pm \nu_c \cos\alpha)^{-2} T_e^{-1.5} \times \ln\left(\frac{4.7 \times 10^{10} T_e}{\nu}\right) \rm EM\ , \quad (1)$$

and the optical depth of thermal gyroresonance emission is

$$\tau_{\rm gr} = 0.052 \frac{s^{2s}}{2^{s+1} s!} n_e \nu^{-1} L_B (1.77 \times 10^{-10} T_e)^{s-1} \times (1 \pm \cos\alpha)^2 \sin^{2s-2}\alpha\ , \quad (2)$$

where T_e is the plasma electron temperature, ν is the observing frequency, EM is the column emission measure (defined as $\int n_e^2\, dl$, the integration along the line of sight), ν_c is the cyclotron frequency ($\nu_{c,\,\rm MHz} = 2.8 B_G$, where B is the strength of magnetic field), α is the angle between the magnetic field and the line of sight, s is the harmonic number ($s = \nu/\nu_c$), and L_B is the magnetic scale height (Kundu 1965). The plus-minus signs ($\pm$) refer to the properties of the two natural modes of the plasma, the extraordinary (X) and ordinary (O) modes; the difference between the modes affects the observed polarization of the radio emission. In the solar radio application, where the Rayleigh-Jeans limit is satisfied (photon energy is far less than the electron thermal energy), it is convenient to express the intensity of radio flux as a brightness temperature T_b, and we use this quantity in the following discussions. In an isothermal plasma, T_b is related to the plasma temperature T_e by

$$T_b = T_e(1 - e^{-\tau})\ , \quad (3)$$

where $T_b = T_e$ when the optical depth $\tau \gg 1$.

In the quiescent corona, the radio flux can be due to thermal bremsstrahlung emission, as well as to thermal gyroresonance emission, if strong magnetic fields are present. In the absence of a complete magnetic model for the corona, we are only able to predict the contribution to T_b from thermal bremsstrahlung emission and thus cannot compare our predictions with radio data in regions where gyroresonance opacity may be significant. We will show that, for the active regions selected in this study, the radio emission is mostly thermal bremsstrahlung emission; the sources with additional thermal gyroresonance emission are excluded in the analysis.

In predicting T_b, we further assume that the emission is optically thin ($\tau \ll 1$), which makes the calculated value of

T_b proportional to the emission measure. This assumption will be justified post hoc on the basis of the radio observations. The predicted T_b for an optically thin isothermal plasma can be simply related to the EM from

$$T_b = 0.2\nu^{-2}T^{-1/2}\mathrm{EM}\ . \quad (4)$$

In the two–temperature-component model, which treats coronal plasma as two isothermal components, the predicted T_b should be

$$T_b = 0.2\nu^{-2}(T_C^{-1/2}\,\mathrm{EM}_C + T_H^{-1/2}\mathrm{EM}_H)\ . \quad (5)$$

Using this formula, we predict T_b at a given wavelength on a pixel-by-pixel basis over the solar disk. The predicted model radio images are shown in Figures 2 and 3, along with the observed radio images.

3.1.2. *Comparison of EIT and VLA Observations at* 20 cm

To obtain a high-quality radio image using the VLA, it is necessary to make a synthesis image using *u-v* coverage over the entire 10 hr observational period. In doing so, we need to take into account the smearing of 20 cm observations by solar rotation. Typically, at 20 cm, at which the full solar disk is in the VLA's field of view, the VLA tracks the center of the Sun's disk without taking any account of solar rotation. Over 10 hr, features at disk center move about 100″ westward, relative to features at the limb, because of rotation, a distance greater than the synthesized beam size. We have exploited a split-merge method to overcome the smearing effect: over successive 4 hr periods, three individual images were made, each of which was rotated to a common time and then merged to obtain the final image. In order to make a valid comparison between the EUV and radio observations, three further steps are needed. First, we need to align the merged radio image with the model radio image. The model radio image is a real snapshot image at about 19:30 UT, while the merged radio image is a simulated snapshot image whose timing corresponds to 18:00

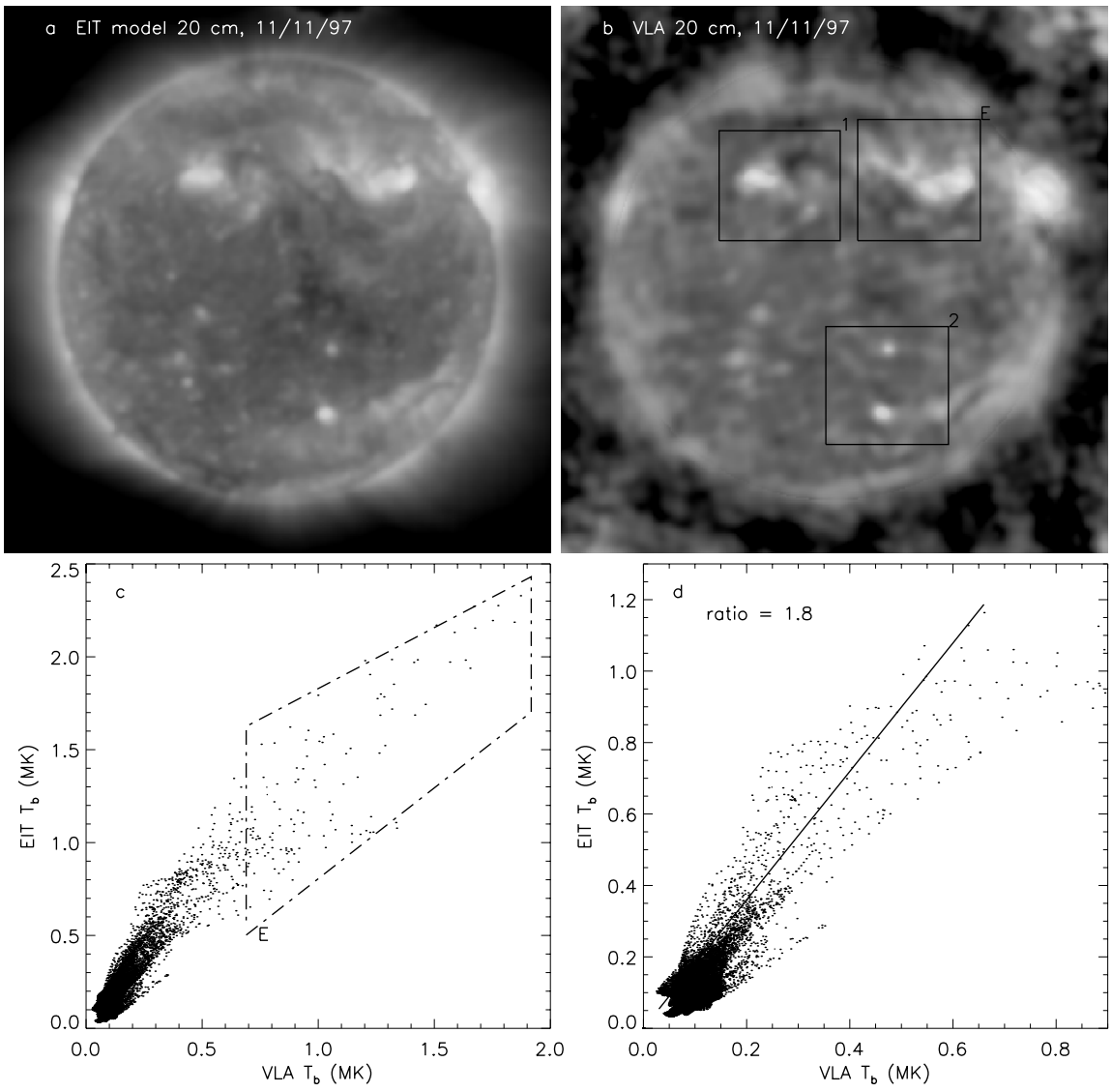

FIG. 2.—Comparison between (*a*) the EIT model T_b image and (*b*) the VLA-observed T_b image at 20 cm on 1997 November 11. The three boxes in (*b*) indicate the locations of active regions individually observed by the VLA at 6 cm. (*c*) Pixel-by-pixel correlation plot between the EIT model T_b (*Y*-axis) and the VLA-observed T_b (*X*-axis) for all pixels within 0.8 $R_\odot$. The size of a pixel is 8″ × 8″. The points in the box (E), which show excessive radio flux, correspond to the bright pixels in the active region labeled "E" in (*b*); the excessive radio flux is contributed by thermal gyroresonance emission in strong magnetic field region i.e; slope value. (*d*) Same as (*c*), but excluding the pixels from region E of (*b*). The solid line represents a linear fit to the correlation, whose slope value is 1.8.

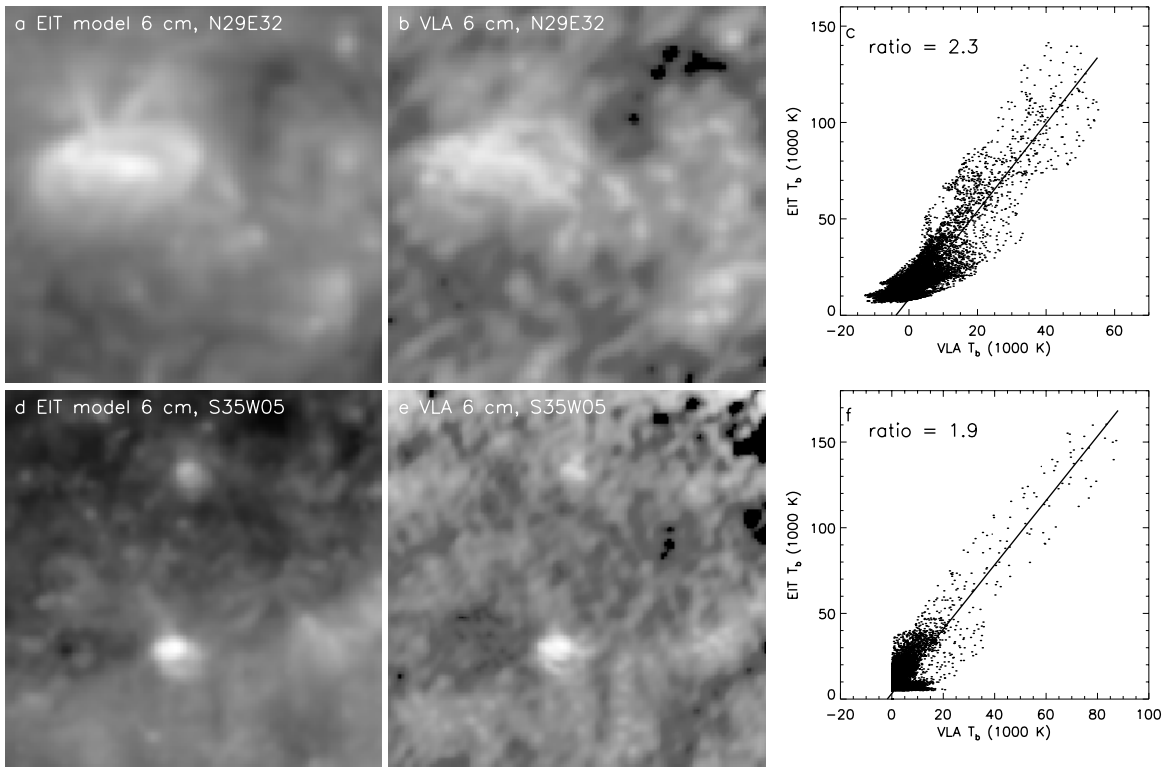

FIG. 3.—Comparison between the EIT model T_b image and the VLA-observed T_b image at 6 cm on 1997 November 11. From left to right in each row, the three panels show the EIT model T_b image, the VLA T_b image, and the plot of their pixel-by-pixel correlation, respectively. The top and bottom rows are for the source N29 E32 (active region labeled "1" in Fig. 2*b*) and source S35 W05 (active region labeled "2" in Fig. 2*b*). The displayed fields of view of the source N29 E32 and S35 W05 are 400″ × 400″ and 450″ × 450″, respectively. Pixel size is 4″ × 4″. Lines in (*c*) and (*f*) represent the linear fit to the correlation.

UT, the middle of the VLA observation period. We rotate the merged VLA image from 18:00 to 19:30 UT in order to have the best alignment. Second, we need to correct for the effect of distance, because the EIT observations were made at the L1 vantage point between the Sun and the Earth, while the VLA observations were at the Earth. We have rescaled the pixel size of EIT to the Earth's distance, in order to make the angular size of the Sun identical; this was achieved by changing the EIT pixel size from 2.″62 to 2.″59. Third, we need to consider the effect of different resolution in the two images. The effective beam size of the VLA 20 cm image is 30″, while the effective beam size of the EIT images, which is equivalent to the size of EIT point-spread function, is 2.″6. The EIT model image is convolved with a Gaussian of dimension $(30^2 - 2.6^2)^{1/2}$, or 29.″9, in order to match the resolution of the VLA 20 cm image.

We are then able to compare the resulting images. The EIT model 20 cm image (Fig. 2*a*) is very similar in appearance to the VLA radio image at 20 cm (Fig. 2*b*). There are three active regions on the disk, which show up clearly in both images (indicated by the boxes in Fig. 2*b*). The filament channel close to the southern polar region is also apparent in both images. This excellent morphological similarity enables us to adopt a pixel-by-pixel correlation method to display the relation between the two images, as shown in Figures 2*c* and 2*d*. Compared with previous studies, which used fluxes summed over an entire observed region, the pixel-by-pixel correlation method dramatically increases the statistical significance. We have excluded pixels close to the limb in the correlation plot, because the limb features on the radio images, which are not snapshot, may have changed significantly as a result of the emergence from behind the limb in the east and occultation behind the limb in the west. The limb-brightening effect in both observations would have further complicated the comparison.

In Figure 2*c*, we show the plot of the EIT model T_b (Y-axis) versus the VLA-observed T_b (X-axis) for all pixels inside 0.8 $R_\odot$. The points, each of which represents a pixel in the images, are well correlated. A perfect match would result in a linear correlation between the predicted and observed values, with a fitted line crossing the zero point. Pixels with radio T_b less than 0.7 MK show roughly this trend, whereas the pixels corresponding to radio T_b greater than 0.7 MK (pixels in the irregular box E of Fig. 2*c*) show a flatter slope, i.e., an excessive radio flux. Careful examination shows that these points are from the brightest part of the active region designated by the box (E) in Figure 2*b*. We believe that the excessive radio flux must be from thermal gyroresonance emission; the region shows high circular polarization, which is consistent with this interpretation. While all pixels have an intrinsic radio flux from the thermal bremsstrahlung emission in the presence of coronal plasma, only those pixels containing strong coronal magnetic field have additional radio flux from the thermal gyroresonance emission. Because we are only interested in reconciling the bremsstrahlung fluxes, we exclude those "contaminated" pixels from the following discussion. Also note that, if the assumption that bremsstrahlung emission is optically thin were violated, we would see points that show a radio flux deficit, i.e., an increase in slope at high T_b. No such effect is seen.

In Figure 2*d*, we simply replot the EIT model T_b versus the VLA T_b for the pixels inside 0.8 $R_\odot$ by excluding the pixels in region E. We fit the points into a single linear

correlation (*solid line*). The value of the slope is 1.8 and the correlation coefficient is 0.87. The value of the slope is significant, which indicates that the predicted T_b is systematically larger than the observed T_b by a factor of 1.8.

3.1.3. *Comparison of EIT and VLA Observations at* 6 cm

Compared with the 20 cm observations presented above, the VLA 6 cm observations are more suitable for quantitative comparison with the EIT observations. First of all, the VLA 6 cm images have a higher spatial resolution, e.g., 13″ in this observation. Second, the thermal bremsstrahlung radio emission at 6 cm is more optically thin, because optical depth (eq. [1]) is proportional to the square of the wavelength. While the 20 cm emission in the corona may be marginally optically thick for strong active regions, the 6 cm emission is always optically thin.

On 1997 November 11, there were four subregions observed by the VLA at 6 cm, alternately pointing at N29 E32, S35 W05, N33 W07, and N21 W73 (the heliospheric position at 0 UT), respectively. The VLA tracked for solar rotation, and smearing should be minimal. The positions of the first three subregions on the solar disk are denoted in Figure 2*b* by "1," "2," and "E," respectively; the last subregion is not denoted, because it is too close to the limb and not considered in this paper. We also discard region E because gyroresonance emission "contaminates" the free-free emission at the core of this active region. In Figure 3, we show the EIT model T_b image, the VLA-observed T_b image, and their pixel-by-pixel correlation for regions 1 (N29 E32; *top panels*) and 2 (S35 W05; *bottom panels*). Again, there is excellent morphological similarity between the model and observed radio images. There exists a good linear correlation between the EIT T_b and the VLA T_b. For the source N29 E32, the linearly fitted slope is 2.3 (correlation coefficient of 0.88; see Fig. 3*c*), while for the source S35 W05, the linearly fitted slope is 1.9 (correlation coefficient of 0.89; see Fig. 3*f*). Again, the predicted T_b is systematically larger than the observed T_b. Note that the fitted line for each region does not cross the zero point in the X-axis, which represents the radio T_b; the crossing occurs at a negative radio T_b, consistent with the absence of the disk component in the 6 cm radio images.

3.2. *1996 June 29 Observations*

The EIT 171, 195, and 284 Å observations were taken at 23:01 and 23:06 UT on 1996 June 29 and 01:31 UT on 1996 June 30, respectively. Note that the 284 Å observation lagged behind the other two observations by 150 minutes. We have rotated the 284 Å image to the 195 Å observation time in order to satisfy the accurate spatial alignment required in the model calculation. Over the 150 minute period, the corona did not undergo significant changes, especially for the large-scale structures such as active regions. We used these three images to derive the temperature and emission measure distribution of the corona with the two–thermal-component model and then calculated the model radio images (Figs. 4*a* and 4*d*) using the methods described in § 3.1.1.

The radio observations were made from 13:30 to 21:38 UT on 1996 June 29 with the VLA, which alternately observed the Sun at 20 cm and 6 cm, in both cases pointing at the center of the disk. The VLA was in its D configuration. The beam size at 20 cm was 40″ × 40″, while at 6 cm it was 18.″8 × 15.″8. We used the split-merge method

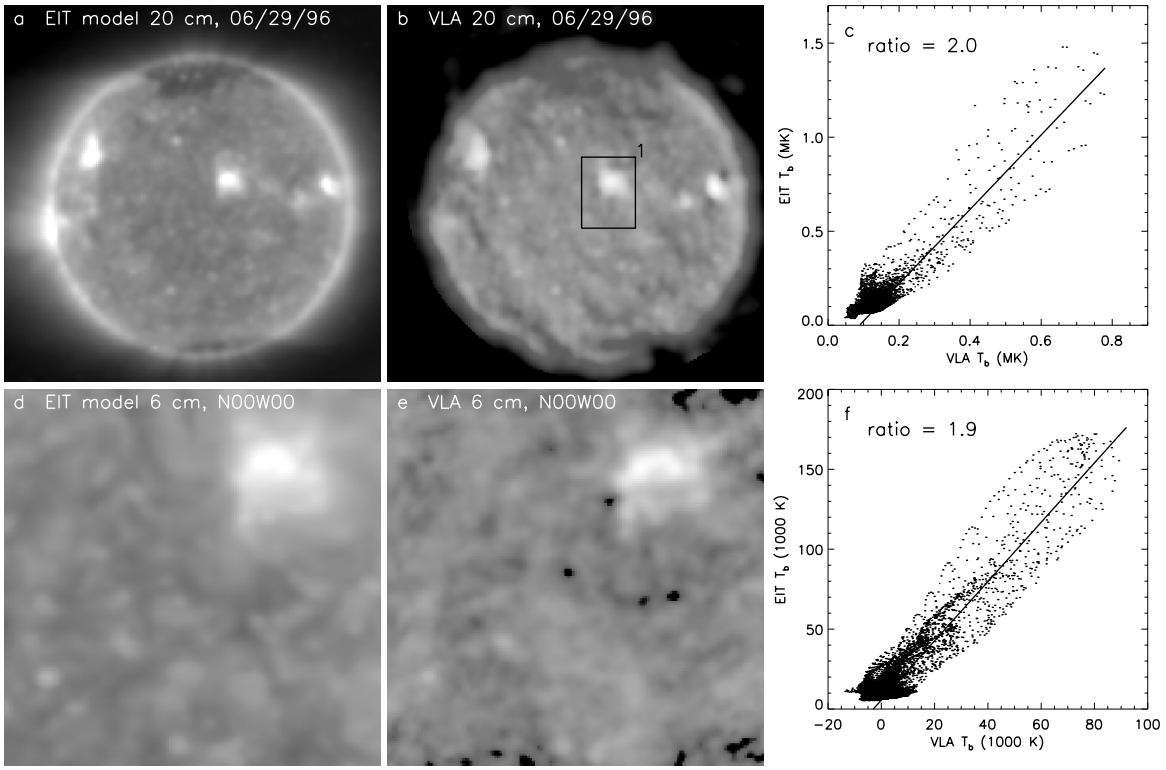

FIG. 4.—Comparison between the EIT model T_b image and the VLA-observed T_b image on 1996 June 29. (*a–c*) EIT model T_b image at 20 cm, VLA-observed T_b image at 20 cm, and the plot of their pixel-by-pixel correlation for pixels within 0.8 $R_\odot$, respectively. Pixel size is 12″ × 12″. The box (1) in (*b*) indicates the source of the VLA observation at 6 cm. (*d–f*) EIT model T_b image at 6 cm, VLA-observed T_b image at 6 cm, and their T_b plot, respectively. The field of view is 600″ × 600″. Pixel size is 4″ × 4″. Lines in (*c*) and (*f*) show the linear fit to the correlation.

described above to compensate for solar rotation. The final image was rotated to the EIT observation time. Although the EIT snapshot observations were made a few hours after the radio observations, the resulting images show that good morphological agreement still exists between the two sets of observations (Fig. 4). In Figure 4*c*, we plot the model T_b versus the observed T_b at 20 cm for all the pixels inside 0.8 $R_\odot$. The solid line is a linear fit to the points, which represent the pixels in the two images. The value of the slope is 2.0 (with a correlation coefficient of 0.86).

Only one source was observed at 6 cm, corresponding to heliospheric position N00 W00 at 0 UT (designated by box 1 in Fig. 4*b*). We show its EIT model image, its VLA-observed image, and their pixel-by-pixel T_b plot in Figures 4*d*–4*f*, respectively. There is a good linear correlation between the two observations. The fitted slope is 1.9 (with a correlation coefficient of 0.82).

3.3. *1996 July 6 Observations*

The instrument configurations and observing time sequences of the EIT and the VLA on 1996 July 6 are similar to those on 1996 June 29. The EIT and VLA images have been processed following the same procedures as in previous examples. In Figure 5, we show the EIT model image, the VLA-observed image, and their pixel-by-pixel T_b correlation plot at 20 cm (*top panels*) and 6 cm (*bottom panels*). Note that the radio image was synthesized from 14:00 to 18:00 UT only, although the VLA observations ended at about 24 UT. By doing so, we avoid the emerging flux region denoted by box E in Figure 5*a*. In this region, magnetic flux rapidly emerged after 18:00 UT, and the radio images also quickly evolved and brightened over hours (White, Lee, & Kundu 1998). The EIT images are snapshots taken after the new flux emerged. Because of the nature of the rapid change of this region, it is not appropriate to include it in the correlation analysis.

The linear correlation between the model and observed T_b is good at both 20 cm (Fig. 5*c*) and 6 cm (Fig. 5*f*) observations. At 20 cm, the linear fit yields a slope of 2.1, with a correlation coefficient of 0.90. There was only one source observed with the VLA at 6 cm, which was centered at S09 E21, as indicated by box 1 in Figure 5*b*. For this source, the linear analysis yields a slope of 1.9, with a correlation coefficient of 0.76.

3.4. *Summary of Observational Results*

We summarize the results of the analysis in Table 1. The five columns in the table indicate the date of observations, the wavelength of radio observations, the source region, the T_b ratio (or the slope of linear fit to the correlation between predicted and observed T_b), and the maximum T_b observed by the VLA. At 20 cm, the source regions used in the analysis are disk pixels within 0.8 $R_\odot$ from the disk center,

TABLE 1

COMPARISON OF MODEL T_b AND OBSERVED T_b

Date	λ (cm)	Source	T_b Ratio	Maximum T_b (K)
1996 Jun 29	20	Full-disk	2.0	8.0×10^5
	6	N00 W00	1.9	9.0×10^4
1996 Jul 6.....	20	Full-disk	2.1	5.5×10^5
	6	S09 E21	1.9	6.5×10^4
1997 Nov 11.....	20	Full-disk	1.8	8.0×10^5
	6	N29 E32	2.3	5.5×10^4
	6	S35 W05	1.9	9.0×10^4

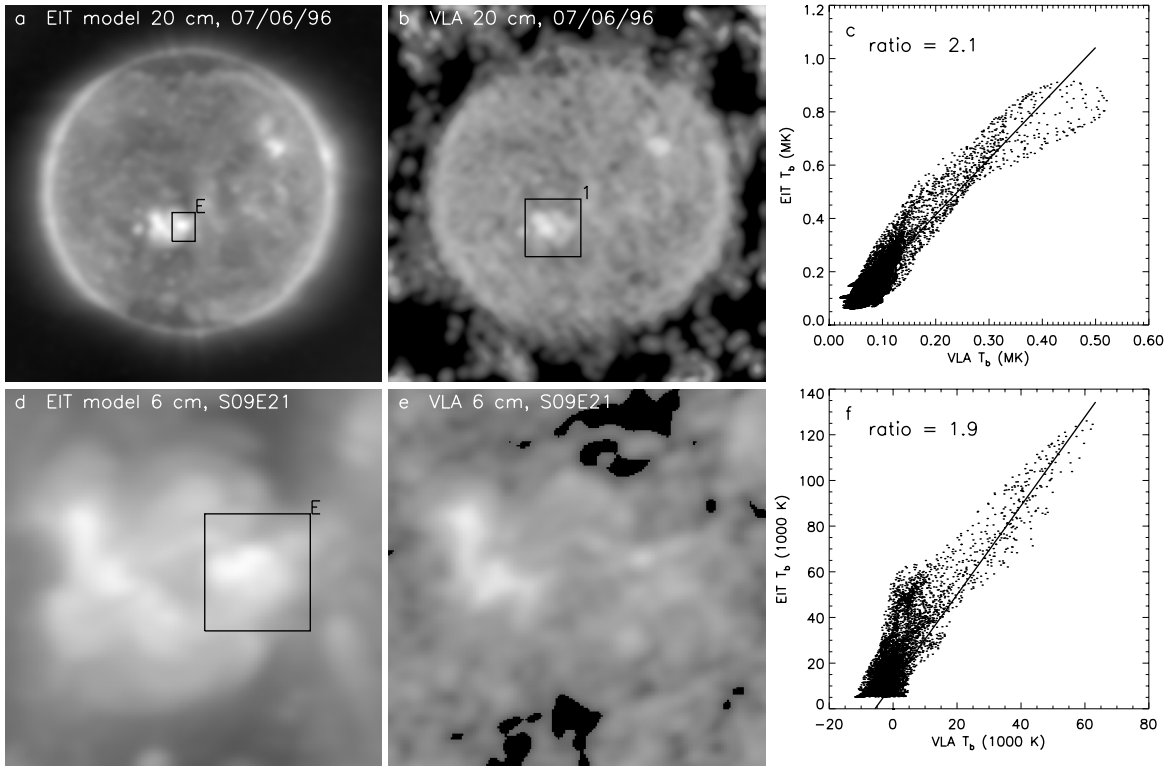

FIG. 5.—Same as Fig. 4, but for 1996 July 6. Pixel size for (*a*)–(*c*) is 10″ × 10″. Field of view for (*d*)–(*f*) is 400″ × 400″. Pixel size is 4″ × 4″. Boxes (E) in (*a*) and (*d*) indicate the new emerging flux region excluded in the correlation analysis. Lines in (*c*) and (*f*) show the linear fit to the correlation.

while at 6 cm the source regions are subregions of several hundred arcseconds, centered at the positions indicated by their heliocentric coordinates in the table. The most important quantitative result from this analysis is the ratio of the two T_b-values. Obviously, the T_b-values predicted from the EIT data are higher than the observed radio T_b-values by a systematic factor, which varies from 1.8 to 2.3 for these observations. The average value of the ratios is 2.0, with a standard deviation σ of 0.2.

The correlation between the EIT–predicted T_b and the VLA-observed T_b is not perfectly linear. There exists a scatter of the pixels in the correlation plot for each observation. One factor that produces scatter is that the EIT data consist of snapshot observations, whereas the VLA data are time-averaged observations, and the studied coronal features vary with time. As mentioned above, each radio image is synthesized over a period of 10 hr of observation. Over this period, the coronal features undergo many minor changes, e.g., transient brightenings and microflares. These changes are time-averaged in the radio observations but not in the EIT data. We expect the predominant effect to be the presence in the EIT data of transient bright features that are absent in the radio images, and these will appear in the correlation plots as points with anomalously large EIT–predicted to VLA-observed T_b ratios. This effect can bias the slopes to large values, but it is difficult for us to assess the significance of this effect, and if only a small number of pixels brighten in a given snapshot observation we do not expect them to dominate our results. In cases where the coronal features are known to undergo significant changes, we simply exclude these features from our analysis, e.g., the region N33 W07 on 1997 November 11 (box E in Fig. 2*b*) and the newly emerging flux region on 1996 July 6 (box E in Figs. 5*a* and 5*d*; also see White et al. 1998). The activity of coronal features can be monitored by the level of *GOES* soft X-ray flux and by the EIT and VLA observations themselves.

The VLA observations used in this study were all taken in the D configuration, which is the most compact one. When we try to explore the observations on 1997 August 3, when the VLA was in its C configuration with a larger antenna separation, we find that the derived T_b ratios are 4.6 at 20 cm and 2.9 at 6 cm, significantly larger than that in the D-configuration observations. One possible contribution to this difference is the fact that the C-configuration data are less sensitive to large spatial scales because of the lack of sufficiently small baselines when the VLA is in the C configuration: the flux from coronal structures with large spatial scales is resolved out by the interferometer. We plan to further investigate this difference in the future with more observations in both D and C configurations.

4. DISCUSSION

In an ideal situation, the model T_b of the EIT observations should be equal to the observed T_b of the VLA. In other words, the T_b ratio should equal 1. However, our analysis showed the following relationship between the model T_b (T_{b_M}) and the observed T_b (T_{b_O}):

$$T_{b_M} = \beta + \alpha T_{b_O} . \quad (6)$$

Although the two T_b-values have a good linear correlation, the ratio factor α is not 1. Instead, $\alpha = 2.0 \pm 0.2$, as presented above. Further, β is sometimes not zero, especially for 6 cm observations. The nonzero value of β is caused by the nature of the radio observation and by the deconvolution technique used in processing the radio images. Because we have exploited a pixel-by-pixel correlation method, the nonzero value of β does not change the value of the slope and thus of the T_b ratio.

The cause of the systematic difference between the predicted and observed T_b-values is most likely an error in the coronal abundances used to predict the radio flux from the EIT data. It is now widely believed that low-FIP elements are overabundant in the corona, whereas the Meyer coronal abundances assume that low-FIP elements in the corona are at photospheric abundance while high-FIP elements are underabundant. As mentioned above, the EIT observations are dominated by EUV photons from highly ionized Fe ions through line emission, while the VLA observations are for radio emission from free electrons. If the true coronal Fe abundance is indeed higher by some factor relative to the value used to obtain the H emission measure, we then overestimate the EUV emission measure and thus the model T_b by the same factor. Therefore, the T_b ratios represent the ratio between the real coronal Fe abundance and Meyer's value. Our numbers put the factor (α) at 2.0, on average. In the absolute abundance term, we place the coronal Fe abundance at 7.8×10^{-5} (Meyer's value is 3.89×10^{-5}; Meyer 1985). In terms of the enrichment factor of Fe abundance in the corona relative to the accepted photospheric value (3.23×10^{-5}; Anders & Grevesse 1989), we place the enrichment factor at 2.4 ± 0.2 (with an observed range from 2.2 to 2.8). For a comparison, we list here the published values of the enrichment factor (and absolute abundance) of Fe in the corona from various sources: 1.2 (3.89×10^{-5}, adopted coronal abundance; Meyer 1985), 3.9 (12.6×10^{-5}, spectroscopic measurements in flares and active regions; Feldman 1992), 9.8 (31.6×10^{-5}, spectroscopic measurements in active regions; Waljeski et al. 1994), 13.1 (42.3×10^{-5}, in situ particle counting; Reames 1999), 1.4 (4.5×10^{-5}, spectroscopic measurements in flares; Fludra & Schmelz 1999), 2.1 (6.74×10^{-5}, proposed hybrid model; Fludra & Schmelz 1999), and 4.8 (15.6×10^{-5}, comparison between EUV and radio observations in active regions; White et al. 2000). Our value for the Fe abundance is closest to the hybrid coronal abundance recently proposed by Fludra & Schmelz (1999), who derived the coronal abundance of various elements based on the mean value of several spectroscopic and particle measurements. This model indicates an intermediate enrichment factor of low-FIP elements in the corona, which is different from the standard models with either a low enrichment factor (about 1; Meyer 1985) or a high enrichment factor (about 4; Feldman 1992; Feldman et al. 1992; Meyer 1993; Feldman & Laming, 2000).

The fact that there exist significantly different coronal abundance models reflects the complexity of the issue. The inconsistency among various studies may be caused by the intrinsic complexity of the objects observed, e.g., the elemental abundance may vary among flaring plasma, active region plasma, and solar energetic particles. Note that our EUV–radio method, in contrast to the spectroscopic method (usually for flaring plasma) and the particle method (usually for solar energetic particles), largely refers to the elemental abundance in quiescent active region plasma. On the other hand, the uncertainties inherited from instrumental calibration and sensitivity, which are often manifested by a large scatter of derived values for a particular method,

could also account for the inconsistency. The scatter of the derived Fe abundance in our method appears smaller than that in most other studies. In the following, we discuss the possible uncertainties in our method caused by instrumental calibration and other factors.

The VLA uses dedicated noise sources for solar calibration, and the temperatures of these noise sources must be measured occasionally in order to ensure that they are appropriate. This introduces some uncertainty in the calibration. In their study, White et al. (2000) were able to assess calibration uncertainties by measuring radio fluxes for the same feature at three independent frequencies, each using different noise sources, thus confirming that the overall calibration was adequate.

A great deal of effort has been put into the EIT calibration using both preflight laboratory measurements and in-flight calibration. Dere et al. (2000) have updated the EIT preflight photometric calibration. In-flight calibration has focused on the degradation of CCD sensitivity because of the strong effect of the EUV photons and the small effect of surface contamination on the CCD. It has been found that the CCD sensitivity may degrade by a factor of 2 over a period of a year and show irregularity between pixels. A comprehensive algorithm (Newmark et al. 2001, private communication) has been developed to compensate for the CCD variation over time and on a pixel-by-pixel basis. The calibrated results are in good agreement with *SOHO* SEM (Solar EUV Monitor) irradiance measurements. It is believed that the overall EIT calibration has an uncertainty less than $\pm 10\%$, with the uncertainty being even smaller for the early EIT observations in 1996 and 1997.

Another uncertainty in our EUV–radio method is due to the limited temperature sensitivity of the EIT bandpasses. The EIT coronal bandpasses are sensitive to the emission of plasma within the temperature range 0.6–2.8 MK, while radio observations see emission from virtually all temperatures (weighted toward cooler temperatures because $T_b \propto T_e^{-1/2}$), as long as the plasma is optically thin. (The coronal features used in this study must be in an optically thin regime, because the maximum T_b observed by the VLA, as shown in Table 1, is less than typical coronal temperatures). Therefore, the radio fluxes predicted from the EIT data may underestimate the true radio fluxes if, e.g., there is a lot of plasma present at $T_e > 3$ MK. But this underestimation should be small, because the emission measure outside the EIT temperature range should be much smaller than that inside the EIT temperature range for the active regions used in this study. There is no doubt that there is little plasma with temperature less than 0.8 MK in an active region. The concern is what fraction of plasma hotter than 3 MK exists in an active region. A direct answer to this question requires a determination of a DEM (Differential Emission Measure) measurement for the region. It has been shown that for typical nonflaring active regions a major amount of plasma is cooler than 3 MK; see, e.g., the active region DEM distributions of Brosius et al. (1996) and Dere & Mason (1993). Recently, based on CDS observations (Coronal Diagnostic Spectrometer on *SOHO*), White et al. (2000) derived the DEM of the active region S35 W05 on 1997 November 11 and found that there is little hot plasma (>3 MK) existing in that region. Thus, we believe that for quiescent active regions, as used in this study, the majority of plasma should reside in the temperature range below 3 MK, which is well sampled by the EIT data. In addition, considering that the radio flux is less sensitive to hotter plasma than to cooler plasma, the effect of hotter plasma is further minimized. A conservative estimation of the uncertainty in the predicted T_b ratios caused by the limited EIT sensitivity range is $+20\%$ for the upper limit and -0% for the lower limit. A better EIT temperature-sensitivity range would make the predicted radio flux even larger.

Because of the complicated convolution of emission measure with plasma emissivity and input photons with instrumental response, it is difficult to derive a simple algorithm to propagate the uncertainties discussed above. Here we simply add the uncertainties together ($\pm 10\%$ for calibration, and $+20\%/-0\%$ for limited EIT temperature-sensitivity range), resulting in an overall uncertainty of $+30\%$ for the upper limit and -10% for the lower limit. This uncertainty places the enhancement factor of the Fe abundance in the corona, relative to the photospheric value, in the range of 2.1 (the lower limit) to 3.1 (the upper limit). These uncertainties are largely in agreement with the uncertainties present in the real observations, which show the enhancement factor in the range from 2.2 to 2.8.

We must also address the difference between our result (Fe enhancement factor of 2.4) and that of White et al. (2000; Fe enhancement factor of 4.8), who used a technique similar to ours. White et al. (2000) made use of the observations of the active region centered at S35 W05 on 1997 November 11, one of many sources used in our study (see Figs. 2 and 3). While they used the same VLA radio observations, they used different EUV observations, namely, spectroscopic observations by CDS. The CDS observations have the advantage of having enough spectral lines (Fe X–Fe XVII inclusive) to calculate a DEM distribution for the corona with better temperature coverage. To check the intercalibration between CDS and EIT, we use the same atomic database (CHIANTI 3.01; Dere et al. 1997), ionization equilibrium equation (Arnaud & Raymond 1992), and coronal elemental abundances (Meyer 1985) to carry out the necessary calculations for both CDS and EIT. The CDS calibration used for this calculation is the version in the CDS software in 2001 May. The CDS data are analyzed by fitting line profiles to individual lines, determining fluxes from the fitting procedure and then using CHIANTI procedures to determine a DEM for the active region that reproduces the observed line fluxes. No spatial background subtraction was carried out for this comparison. However, the flux of the entire active region has to be summed to make a single DEM distribution, in order to enhance the signal-to-noise ratio. We then predict the EUV flux of that active region in each EIT channel, based on the DEM distribution derived from the CDS observations of the same region. We find that the flux predicted from the CDS observations is larger than that observed by EIT by factors of 1.8 at 171 Å, 1.9 at 195 Å, and 1.2 at 284 Å. These results are roughly consistent with the difference between the abundances inferred from the EIT and CDS data. However, we also find that the results are quite sensitive to additional factors. In particular, the emissivities of the Fe IX and Fe X lines changed between earlier and later versions of CHIANTI. This has a substantial effect on the amount of cool material inferred at $\log T = 5.9$, which contributes to the 171 Å EIT channel: in newer versions of CHIANTI it decreases by an order of magnitude, compared with CHIANTI 0.9, and thus dramatically reduces the predicted

171 Å flux. This example emphasizes the fact that the uncertainties in predicting the flux from a single line are much more dependent on the quality of the atomic data for that line than are integrated quantities, which depend on a number of lines. We are at present unable to reconcile our result for the Fe abundance with that of White et al. (2000) to better than 70%: the difference can be due to the atomic data used in determining the DEM and calculating line fluxes or to the calibration of either CDS or EIT. The relative calibration of EIT and CDS is the subject of ongoing effort.

In the early studies, which compared radio observations with soft X-ray observations of the corona, it was suggested that the discrepancy between the predicted and observed radio fluxes may be due to the existence of cool material ($\sim$0.5 MK; Nitta et al. 1991; Brosius et al. 1992; Schmelz et al. 1992, 1994). The assumed cool material, which sits between the active region plasma and the observer, would be transparent to the EUV and soft X-ray photons, but it would significantly absorb the radio emission from the underlying active regions. Though this assumption is an option to explain the discrepancy, it is not justified on observational grounds. The observations of active regions by the CDS reveal that cool material only exists inside active region loops and in a transient manner, with a lifetime of tens of minutes (see, e.g., Brekke, Kjeldseth-Moe, & Harrison 1997). Apparently, there is insufficient cool material existing above active regions to explain the discrepancy between EUV and radio fluxes. We therefore argue that the abundance effect should be a viable explanation for the difference between radio and EUV/soft X-ray observations.

5. CONCLUSION

In this paper, we have made a quantitative comparison between imaging observations of the corona in two different spectral domains: one at EUV wavelengths by the EIT, the other at radio wavelengths by the VLA. There are, in total, seven observations investigated. There exists excellent morphological similarity between the EUV and radio observations. This indicates that both observations are sensitive to the same solar feature: the million-degree coronal plasma. The images of the EIT and the VLA largely outline the emission measure distribution of the corona, which may vary by over 3 orders of magnitude.

We predict the radio flux (or brightness temperature) distribution of the corona from the emission measure and temperature derived from the multiple-channel EIT observations. The radio images thus determined are compared with the radio images observed by the VLA. Exploiting a pixel-by-pixel correlation method, we have shown that there exists good linear correlation between the predicted and observed radio fluxes applying to different coronal features. However, the predicted radio flux is systematically higher than that observed by a factor ranging from 1.8 to 2.3; the average of the ratio of the radio flux is 2.0 ± 0.2.

We attribute this difference to the use of the adopted coronal abundance of Meyer (1985), whose Fe abundance is underestimated. Our result suggests that the Fe abundance in the corona (specifically, in the quiescent active regions) is 2.0 times as large as Meyer's value: 7.8×10^{-5} in the common format. In terms of the enrichment factor of low-FIP elements in the corona relative to the photospheric value, we place it at 2.4, which is close to the recently proposed hybrid coronal abundance model (Fludra & Schmelz 1999) but not to the standard low-enrichment model (Meyer 1985) or high-enrichment model (Feldman 1992).

This research was supported by NASA grants NAG 5-6257, NAG 5-7901, and NAG 5-7373 and NSF grant ATM 96-12738. J. Z. thanks A. Nindos for valuable discussions. The VLA is a facility of National Radio Astronomy Observatory, operated by Associated Universities, Inc. under contract with the National Science Foundation. *SOHO* is a project of international cooperation between ESA and NASA.

REFERENCES

Anders, E., & Grevesse, N. 1989, Geochim. Cosmochim. Acta, 53, 197
Arnaud, M., & Raymond, J. 1992, ApJ, 398, 394
Brekke, P., Kjeldseth-Moe, O., & Harrison, R. A. 1997, Sol. Phys., 175, 511
Brosius, J. W., Davila, J. M., Thomas, R. J., & Monsignori-Fossi, B. C. 1996, ApJS, 106, 143
Brosius, J. W., Davila, J. M., Thomas, R. J., & White, S. M. 1997, ApJ, 488, 488
Brosius, J. W., Willson, R. F., Holman, G. D., & Schmelz, J. T. 1992, ApJ, 386, 347
Delaboudinière, J.-P., et al. 1995, Sol. Phys., 162, 291
Dere, K. P., Landi, E., Mason, H. E., Monsignori-Fossi, B. C., & Young, P. R. 1997, A&AS, 125, 149
Dere, K. P., & Mason, H. E. 1993, Sol. Phys., 144, 217
Dere, K. P., et al. 2000, Sol. Phys., 195, 13
Feldman, U. 1992, Phys. Scr., 46, 202
Feldman, U., & Laming, J. M. 2000, Phys. Scr., 61, 222
Feldman, U., Mandelbaum, P., Seely, J. F., Doschek, G. A., & Gursky, H. 1992, ApJS, 81, 387
Fludra, A., & Schmelz, J. T. 1999, A&A, 348, 286
Klimchuk, J. A., & Gary, D. E. 1995, ApJ, 448, 925
Kundu, M. R. 1965, Solar Radio Astronomy (New York: Interscience)
Meyer, J.-P. 1985, ApJS, 57, 173
———. 1993, Adv. Space Res., 13(9), 377
Moses, D., et al. 1997, Sol. Phys., 175, 571
Nitta, N., et al. 1991, ApJ, 374, 374
Reames, D. V. 1999, ApJ, 518, 473
Schmelz, J. T., Holman, G. D., Brosius, J. W., & Gonzalez, R. D. 1992, ApJ, 399, 733
Schmelz, J. T., Holman, G. D., Brosius, J. W., & Willson, R. F. 1994, ApJ, 434, 786
Waljeski, K., Moses, D., Dere, K. P., Saba, J. L. R., Strong, K. T., Webb, D. F., & Zarro, D. M. 1994, ApJ, 429, 909
Webb, D. F., Holman, G. D., Davis, J. M., Kundu, M. R., & Shevgaonkar, R. K. 1987, ApJ, 315, 716
White, S. M. 1999, Sol. Phys., 190, 309
White, S. M., Lee, J., & Kundu, M. R. 1998, in ASP Conf. Ser. 155, Three-Dimensional Structure of Solar Active Regions, ed. C. E. Alissandrakis & B. Schmieder (San Francisco: ASP), 130
White, S. M., Thomas, R. J., Brosius, J. W., & Kundu, M. R. 2000, ApJ, 534, L203
Zhang, J., White, S. M., & Kundu, M. R. 1999, ApJ, 527, 977